










Transport and acceleration mechanism of fast ions during edge localized modes in ASDEX Upgrade

J.F. Rivero-Rodríguez^{1,*} , J. Galdon-Quiroga² , J. Domínguez-Palacios²,
M. García-Muñoz² , D. García-Vallejo³, J. Gonzalez-Martin³, K.G. McClements¹ ,
L. Sanchís⁴ , K. Särkimäki⁴ , A. Snicker⁴ , Y. Todo⁵ , L. Velarde⁶, E. Viezzer² 
and the ASDEX Upgrade Team^a

¹ United Kingdom Atomic Energy Authority, Culham Centre for Fusion Energy, Culham Science Centre, Abingdon, Oxon OX14 3DB, United Kingdom of Great Britain and Northern Ireland

² Departamento de Física Atómica, Molecular y Nuclear, Universidad de Sevilla, Sevilla, Spain

³ Departamento de Ingeniería Mecánica y Fabricación, Universidad de Sevilla, Sevilla, Spain

⁴ Department of Applied Physics, Aalto University, PO Box 14199, Espoo FI-00076, Finland

⁵ National Institute for Fusion Science, Toki, Gifu 509-5292, Japan

⁶ Departamento de Ingeniería Energética, Universidad de Sevilla, Sevilla, Spain

E-mail: juan.rivero-rodriguez@ukaea.uk

Received 21 February 2023, revised 3 June 2023

Accepted for publication 29 June 2023

Published 12 July 2023



CrossMark

Abstract

Observations of enhanced fast-ion losses during edge localized modes (ELMs) have been reported in the ASDEX Upgrade tokamak, revealing losses above the injection energy. This suggests that fast ions can be accelerated and lost due to the ELMs. Recent analysis of the ELM-induced losses suggests that the fast ions are lost due to a resonant interaction with the electromagnetic perturbation during the ELM crash. The fast-ion transport and acceleration during ELMs is modelled using electromagnetic fields computed using the hybrid kinetic-MHD code MEGA, while fast-ion full orbits are tracked with the ASCOT code. Time-evolving 3D electromagnetic fields have been implemented in ASCOT to compute fast-ion orbits in the presence of fast MHD events such as ELMs. The simulations successfully reproduce a field-aligned pattern of the losses on the tokamak wall and the formation of an accelerated population in the lost fast-ion distribution, while they predict an accelerated population in the confined distribution. A parametric study of the fast-ion constants of motion suggests a resonant interaction between the fast-ions and the electromagnetic fields arising during the ELM crash. In the case of fast-ion acceleration, the perpendicular electric perturbation, with scales smaller than the fast-ion gyroradius, breaks magnetic moment conservation and resonantly modifies the fast-ion energy.

^a See Stroth *et al* 2022 (<https://doi.org/10.1088/1741-4326/ac207f>) for the ASDEX Upgrade Team.

* Author to whom any correspondence should be addressed.



Original Content from this work may be used under the terms of the [Creative Commons Attribution 4.0 licence](https://creativecommons.org/licenses/by/4.0/). Any further distribution of this work must maintain attribution to the author(s) and the title of the work, journal citation and DOI.

Keywords: fusion, tokamak, fast-ions, ELMs, MHD, Monte-Carlo

(Some figures may appear in colour only in the online journal)

1. Introduction

The H-mode, planned as the baseline operational scenario for ITER, is a high-confinement regime in tokamak plasmas characterized by a steep pressure gradient at the edge, referred to as a pedestal. Above a certain limit, determined by the peeling-ballooning stability boundary [1], the plasma exhibits explosive and semi-periodic electromagnetic perturbations, known as edge localized modes (ELMs) [2]. ELMs collapse the plasma pedestal, causing a burst of energy and density to the tokamak wall that is expected to be intolerable during sustained operation in future devices [3, 4]. Recent experiments in the ASDEX Upgrade tokamak have revealed accelerated beam-ion losses correlated with a particular category of ELM referred to as *type I* [5, 6]. The experiments give clear evidence that the fast ions are accelerated and their losses increased by the ELM perturbation, although the particular mechanism by which fast ions are transported and accelerated is still largely unknown. Understanding ELM-induced fast-ion losses and acceleration is important as neutral beam injection (NBI) provides a strong source of fast ions close to the plasma edge, resulting in a large amount of energy whose confinement in the plasma is vulnerable to edge instabilities like ELMs. In previous studies, it was proposed that the fast-ion transport and acceleration mechanism involved a resonant interaction between the fast-ion orbits and the electromagnetic perturbation during an ELM. The proposed cause for fast-ion acceleration was an electric field parallel to the magnetic field lines arising during magnetic reconnection events, that are believed to occur during ELM crashes [7]. Observations of electron acceleration during magnetic reconnection events in MAST [8, 9] and AUG [6] appear to support this hypothesis. However, a preferential acceleration parallel to the magnetic field would reduce the pitch angle ($\Lambda = \arccos(\frac{v_{\parallel}}{v})$) of the accelerated fast ions. If we assume that the accelerated fast-ion losses have the same source as the prompt-losses measured by fast-ion loss detector (FILD), an acceleration solely due to a parallel electric field could be in conflict with the experimental observations as the pitch-angle of the accelerated fast ions remained comparable to those of the NBI prompt losses. A recent paper proposed that the fast ions undergo a gyrotron acceleration process induced by the vertical polarization of outward-propagating ELM filaments with sizes smaller than the fast-ion gyroradius [10]. The proposed mechanism would complement the parallel acceleration, thus keeping a constant pitch-angle structure.

This paper aims to explore the mechanism by which fast ions are transported and accelerated during an ELM. It provides new experimental data, resolving the poloidal fast-ion loss distribution and the effect of the plasma q_{95} on the losses, where q_{95} is the safety factor at the normalised minor radius $\rho_{\text{pol}} = 0.95$ (defined in terms of the poloidal magnetic field). ρ_{pol} is the square root of normalised poloidal flux. This work also combines for the first time

magnetohydrodynamic (MHD) simulations from the hybrid kinetic-MHD code MEGA [11, 12] and fast-ion orbit simulations from the Monte-Carlo orbit-following code ASCOT [13]. The numerical results quantify for the first time the effect of ELMs on the confined and lost fast-ion distributions using realistic MHD simulations to compute the electromagnetic perturbation, in contrast with the analytical perturbation prescribed in previous studies [5, 6]. The full-orbit simulations of the fast ions use a time-evolving 3D description of the electromagnetic perturbation. The results make it possible to reproduce the main experimental observations in ASDEX Upgrade. A parametric study of variations in the fast-ion constants of motion in unperturbed fields (toroidal canonical momentum and energy) and the magnetic moment is used to investigate the resonant transport and acceleration produced by the electromagnetic perturbation.

The paper is structured as follows: section 2 covers the most recent experimental observation of ELM-induced fast-ion losses in ASDEX Upgrade. In section 3, the MHD simulations from MEGA combined with the full-orbit simulations from ASCOT are presented and used to estimate the losses induced by the ELM perturbation. Then, a transport and acceleration mechanism for the ELM-induced fast-ion losses is proposed using a parametric analysis of the fast-ion constants of motion. Lastly, the results are discussed in section 4.

2. Experimental results

The ELM-induced fast-ion losses were first experimentally characterized in AUG using a FILD [14–16]. The FILD probe, located near the last closed flux surface (LCFS) on the low field side (LFS), works as a magnetic spectrometer, collimating the fast ions escaping from the plasma onto a scintillator plate. The fast-ion flux and the velocity space of the losses can be inferred from the intensity and the position of the glowing area on the scintillator plate, respectively. The ELM-induced fast-ion losses are routinely observed as peaks in the FILD time trace, correlated with semi-periodic bursts in the divertor current and the magnetic loop voltage that indicate ELM crashes [17]. This was the first direct evidence of fast-ion losses enhanced by ELMs. More recently, the fast-ion deuterium- α (FIDA) diagnostic [18] has been employed to diagnose the effect of ELMs on the confined fast-ion population, providing further evidence of the loss of fast ions near the plasma edge during an ELM [19].

In previous studies, the signals of two different FILDs in AUG separated 113° toroidally (FILD1 and FILD2) were compared, revealing a non-homogeneous distribution of the ELM-induced losses in the toroidal direction [5, 6]. Now, a FILD poloidal array [20–22] makes it possible to study the poloidal distribution of the losses. This array consists of several FILD probes in different poloidal locations of the wall,

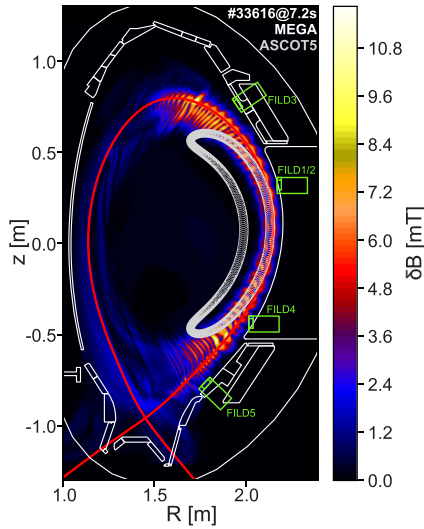


Figure 1. Poloidal cross section of AUG showing a MEGA calculation of the magnetic field perturbation associated with an ELM (colour bar). A fast-ion orbit calculated with ASCOT is in light grey, FILD probes are marked in green and the red curve shows the confined plasma separatrix.

whose positions are illustrated in figure 1. ELM-induced fast-ion losses are not as clearly observed in the probes that are more separated from the midplane (FILD3 and FILD5). Thus, the signals of FILD1 and FILD4, which are in a similar toroidal position but different poloidal positions, are compared. Figure 2(a) shows the outer and inner divertor current, whose peaks are used to monitor the ELM occurrence and duration (shaded grey), figure 2(b) shows the time trace of FILD1 and FILD4 and figure 2(c) shows a closer view of the FILD signals during a single ELM crash. The latter shows that several spikes in the fast-ion losses can be observed during an ELM, which do not occur at the same time or with the same relative amplitude in each probe. This result is very similar to the comparison of toroidally displaced probes reported in previous works, thus suggesting a non-homogeneous distribution of the fast-ion losses not only in the toroidal but also in the poloidal direction. This supports the hypothesis of a 3D filamentary structure of the fast-ion losses during the ELM crash [5, 6].

The velocity-space of the fast-ion losses during an ELM has also been studied in previous works [5, 6]. The intra-ELM velocity-space measurements of the fast-ion losses reveal the presence of a population at energies tens of keV above the primary NBI injection energy, as can be observed in figure 3(a). A tomographic inversion of the measurements provided by the FILDSIM code [23, 24], reproduced in figure 3(b), shows that this accelerated population (which we will refer to as a high-energy feature) is very localized in velocity space. The accelerated population is observed on passing ($\Lambda \sim 45^\circ$, NBI7) and trapped ($\Lambda \sim 60^\circ$, NBI8) fast ions. In an earlier study, a q_{95} scan from 3.7 to 4.3 revealed that the pitch-angles of accelerated passing orbits changed with the plasma

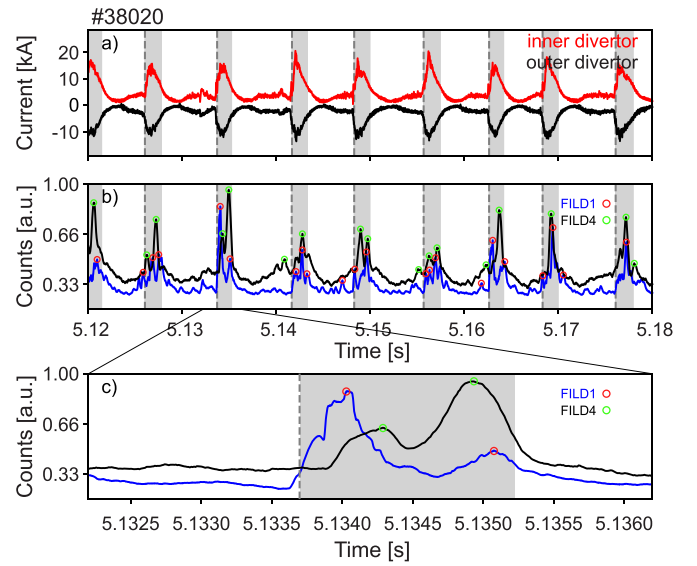


Figure 2. (a) Time trace of the inner and outer divertor current. (b) Time trace of FILD1 and FILD4. The most prominent spikes in the signal are circled. (c) Close-up of FILD1 and FILD4. The times of ELM onset, as measured by the initial rise in the divertor current, are marked by the dashed grey lines and the ELM durations are shaded.

q_{95} , a phenomenon that was referred to as pitch-angle splitting [5, 6]. In the present paper we report the results of a q_{95} scan from 4.8 to 6, to investigate the pitch-angle structure of the accelerated trapped ions. The scan was carried out by ramping B_t from 2.25 T to 2.75 T, while keeping a constant $I_p = 800$ kA. In these shots the high-energy feature of the trapped particles (4.6 cm) was centred on the same pitch angle (67°) as the NBI prompt losses (3 cm), as can be observed in figure 3(c), and did not show any pitch-angle splitting. Therefore, even though the acceleration mechanism affects both trapped and passing orbits, only the passing orbits depict a strong dependency on q_{95} . This result suggests a resonant acceleration mechanism, as the geometrical resonance condition for passing particles depends on the safety factor $\omega_b/\bar{\omega}_d \propto 1/q$ while the trapped-orbit resonances are broader in phase space and do not depend on q explicitly [25, 26]. Here ω_b denotes the bounce frequency (trapped ions) or poloidal transit frequency (passing ions) while $\bar{\omega}_d$ denotes the precessional drift frequency.

A dataset of ELMy H-mode discharges from AUG has been built to carry out a statistical analysis of the ELM-induced losses. This provides a more general understanding of the ELM-induced fast-ion losses and makes it possible to find the parameters that most strongly affect them. The selected shots consist of lower single-null plasmas with $I_p = 800$ kA, $B_t^{axis} = 1.8$ –2.5 T, $n_e^{axis} \sim 6 \cdot 10^{19} \text{ m}^{-3}$, $T_e^{axis} \sim 5$ keV and edge collisionality $0.4 < \nu_e^* < 1.4$. The shots utilise the 8 NBI sources in AUG, each providing 2.5 MW with different injection geometries and energies. The 8 beamlines are separated into two beam boxes: box 1 consist of beams 1–4 and box 2 consists of beams 5–8. The primary injection energy is $E_0 = 60$ keV

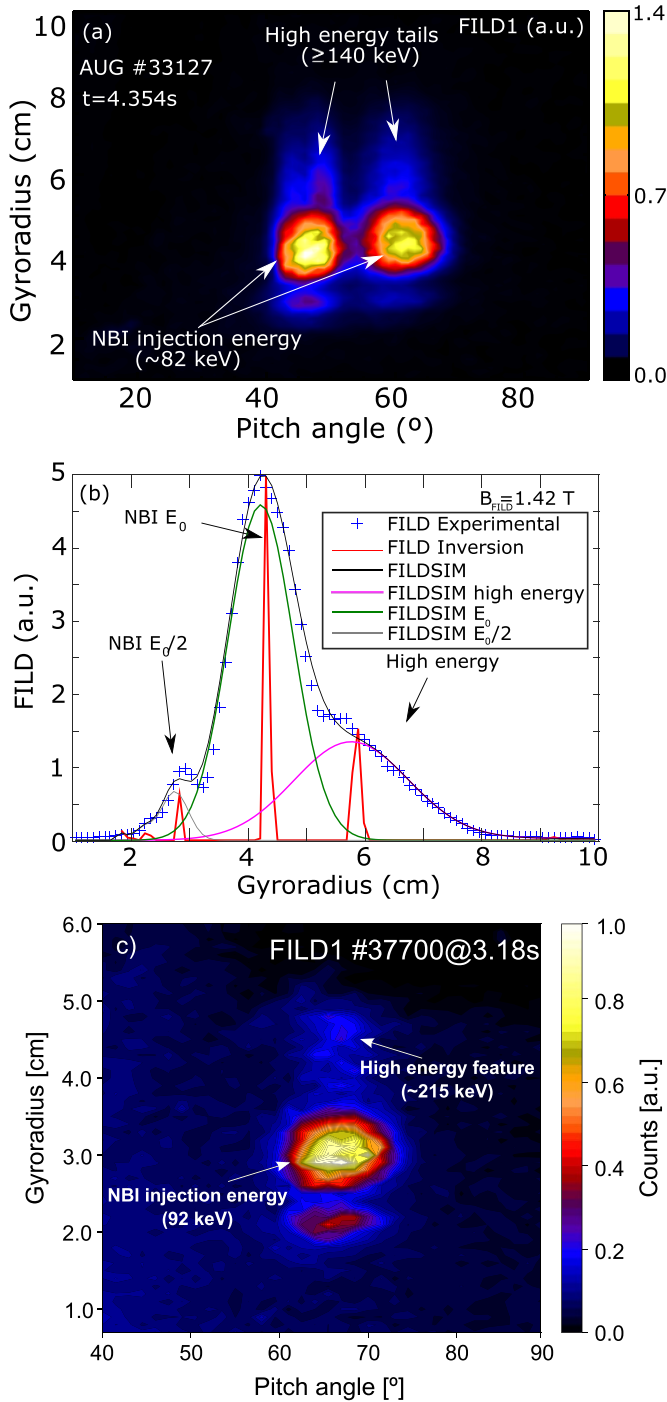


Figure 3. (a) Intra-ELM velocity-space measurements of the fast-ion losses. (b) Gyroradius profile of the intra-ELM measurements between $\Lambda = [58^\circ, 65^\circ]$. The blue crosses correspond to the experimental data, the red curve to the tomographic inversion and the black curve is the reconstructed signal. Reproduced from [5]. CC BY 4.0. (c) Intra-ELM velocity-space measurements of trapped fast-ion losses.

for box 1 and $E_0 = 93$ keV for box 2. Beams 1, 4, 5 are radial,—producing more trapped particles— and beams 2, 3, 6, 7, 8 are tangential,—producing more passing particles—. FILD mostly measures fast-ion losses from box 2. The dataset covers the most recent shots dedicated to investigate ELM-induced fast-ion losses [5, 6, 27] and shots dedicated

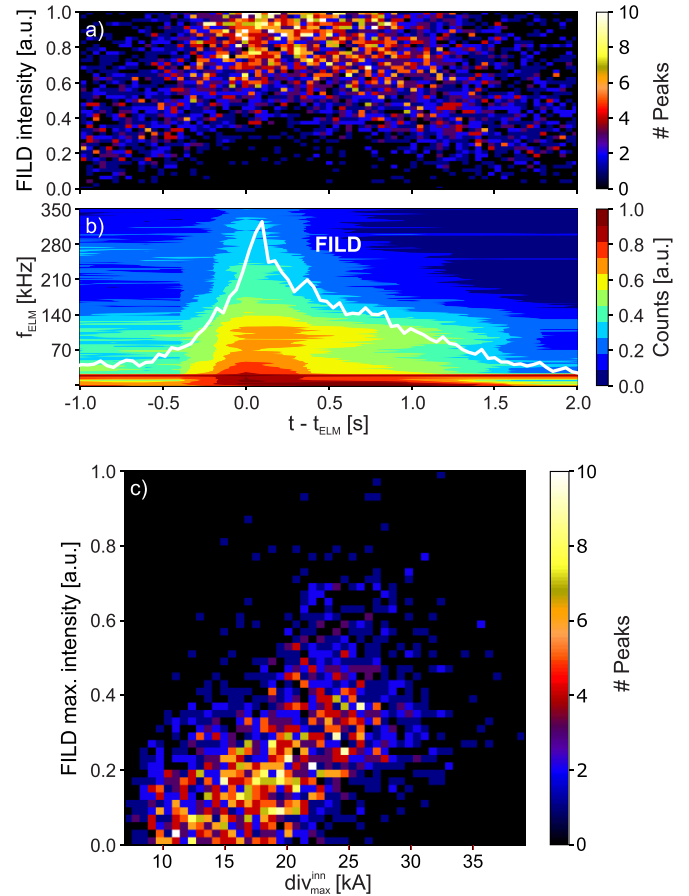


Figure 4. (a) Histogram of the FILD peaks synchronized with the ELM onset from the shots dataset. (b) Spectrogram of the magnetic perturbation synchronized with the ELM onset. (c) Histogram of the maximum divertor current and maximum FILD amplitude from each ELM of the shots dataset.

to ELM mitigation with externally-applied resonant magnetic perturbation (RMP) coils. An algorithm detects the peaks on the FILD signal, as shown in figure 2(b). The peak detection is based on the signal threshold and prominence, whose limits are optimized with a convergency test. A histogram of the peaks relative amplitude synchronized with the ELM onset is shown in figure 4(a). The magnetic perturbation measured with the Mirnov coils, synchronised with the ELM onset [28], is shown in figure 4(b), together with the peaks histogram in FILD. In general, more than one spike per ELM can be observed on the FILD signal. Although most of the peaks with the highest amplitude occur during the ELM crash, when the magnetic perturbation is the highest, some of these spikes occur before the ELM onset, suggesting also a deleterious effect of the ELM precursor on the fast-ion confinement. The peaks histogram is proportional to the magnetic perturbation, showing that the fast-ion transport mechanism is driven by the magnetic perturbation. Figure 4(c) shows a histogram comparing the maximum peak amplitude on FILD and the peak amplitude on the divertor current, which provides a measure of electron losses due to the ELM. This correlation suggests that the ELM-induced fast-ion losses scale with the thermal particle losses.

3. Numerical results

In this section, the electromagnetic perturbation caused by a type-I ELM is modelled with the MEGA hybrid kinetic-MHD code. The resulting electromagnetic perturbation is then fed to the ASCOT5 orbit-following code to solve the fast-ion orbits and assess their acceleration and losses. Finally, the transport and acceleration mechanism will be discussed with a parametric study of the fast-ion orbits constants of motion in ASCOT5.

3.1. Non-linear MHD simulations of an ELM

The electromagnetic perturbation caused by a type-I ELM is computed with the hybrid kinetic-MHD code, MEGA [11, 12]. MEGA describes the bulk plasma using the single-fluid non-linear resistive MHD equations, coupled with the energetic particle kinetic equations via the energetic particle current density. However, the effect of energetic particles is disabled in the simulation presented here. Therefore, only the single-fluid resistive MHD module is employed, as it is a suitable model to calculate the electromagnetic perturbation during an ELM, provided that energetic particles make only a small contribution to the current density. We are thus treating energetic ions as a test particle species in our ELM model. The effect of the fast ions on the ELM instability are being addressed in a separate study [29]. The form of Ohm's law used in MEGA includes the $\mathbf{v} \times \mathbf{B}$ term and the resistivity term:

$$\mathbf{E} = -\mathbf{v} \times \mathbf{B} + \eta(\mathbf{J} - \mathbf{J}_{eq}) \quad (1)$$

where \mathbf{v} is the plasma single-fluid velocity, \mathbf{B} is the magnetic field, η is the plasma resistivity, \mathbf{J} is the plasma current density and \mathbf{J}_{eq} the equilibrium plasma current density. Thus, the MHD module of MEGA can, for example, reproduce the signatures of magnetic reconnection due to large amplitude Alfvénic fluctuations reported in [30]. Parallel electric fields resulting from reconnection have been proposed as the cause of the fast-ion acceleration during the ELM [5, 6]. However, equation (1) neglects terms arising from electron inertia, Hall and diamagnetic effects, limiting to some extent its applicability. MEGA uses 3D cylindrical coordinates that extend beyond the plasma boundaries up to the first wall, thus making it possible to study large drift orbits of confined and lost fast ions near the edge. The diverted plasma shape, shown in figure 1, and the plasma parameters used in the model approximate those of AUG shot #33616 at $t = 7.2$ s,—axial magnetic field $B_t^{\text{axis}} = 2.5$ T, plasma current $I_p = 800$ kA, axial electron density and temperature $n_e^{\text{axis}} = 7.5 \cdot 10^{19} \text{ m}^{-3}$, $T_e^{\text{axis}} = 3.3$ keV—. These parameter values are similar to those of the pulses discussed in section 2, thus making it possible to compare the experimental and numerical results. The resistivity is set to $\eta = 10^{-5} \Omega m$, two order of magnitude above the Spitzer value at the edge, to ensure numerical stability. The resulting magnetic perturbation is shown in figure 1 and the magnetic energy of the perturbation decomposed in toroidal mode numbers is shown in figure 5(a). The simulation successfully reproduces a high n ballooning mode, with a fast growth of low n modes

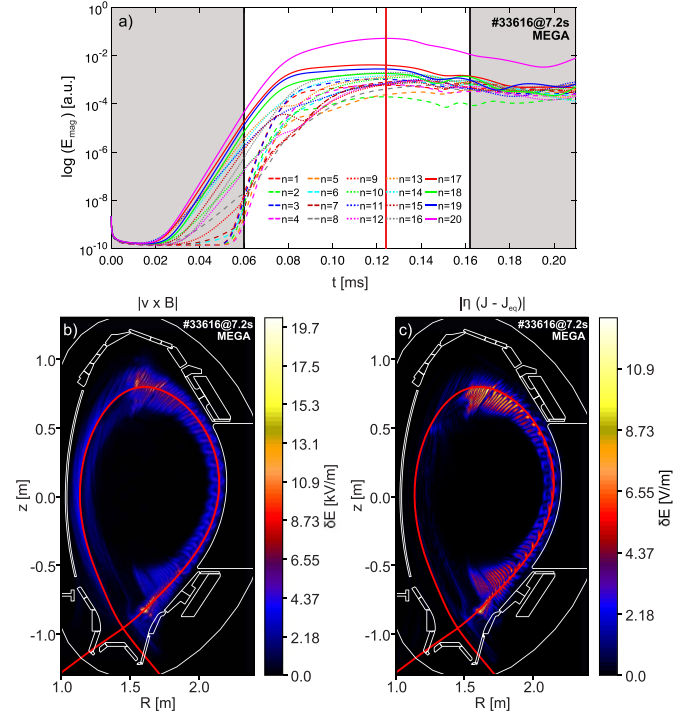


Figure 5. (a) Evolution of the magnetic energy in a MEGA simulation of an ELM in ASDEX Upgrade decomposed in toroidal mode numbers. The unshaded region marks the time window simulated in section 3.2. The red vertical line at $t = 0.125$ ms marks the time step discussed in section 3.3. (b) $\mathbf{v} \times \mathbf{B}$ term of the electric perturbation. (c) Resistive term of the electric perturbation.

due to non-linear coupling. It results in the relaxation of the pressure gradient and generates a filamentary-like electromagnetic perturbation near the edge on the LFS, thus mimicking the main features of a type-I ELM [31]. However, the dominant toroidal mode number is $n = 20$, in contrast to the $n = 3$ and $n = 5$ observed in #33616 and generally in AUG experiments [28]. Also, the growth rate of the perturbation is $\gamma \sim 10^5 \text{ s}^{-1}$, an order of magnitude above that observed experimentally [32]. Both discrepancies are believed to occur due to the neglect of diamagnetic effects in the Ohm's law, which are known to damp higher n numbers and reduce the overall growth rate [33]. Besides, since the growth rate is proportional to the cube root of the plasma resistivity ($\gamma \propto \eta^{1/3}$) [34], a resistivity above the Spitzer value contributes to overestimate the growth rate. The latest JOREK results successfully reproduce the experimental n number using realistic resistivity values and diamagnetic effects [35]. Simulations with such a growth rate lead to a very low effect on the fast ions, as the particles do not have enough time to interact with the mode. Consequently, the growth rate of the MEGA perturbation is artificially reduced by an order of magnitude in ASCOT with the aim of modelling more realistically the effect of the electromagnetic fields on the fast-ion orbits. The duration of the ELM perturbation in MEGA, marked by the unshaded region in figure 5(a), is increased from 0.1 ms to 1 ms by stretching the time input in ASCOT. Considering that the orbital time

scale ranges between 3–8 μs , this change will provide an electromagnetic perturbation whose duration is several hundreds of orbital times. Simulations without the stretch of the perturbation lead to very low statistic results difficult to interpret as the particles do not have enough time to interact with the mode. As mentioned above, the resistive effects are overestimated in the results. Nevertheless, figures 5(b) and (c) show that the resistive term of Ohm's law in MEGA is not dominant in comparison to the $\mathbf{v} \times \mathbf{B}$ term, perpendicular to the magnetic field. The parallel electric field computed by MEGA agrees with JOREK modelling in that they both show high- m field-aligned helical structures near the separatrix with similar order of magnitude [36]. This implies that the electric perturbation resulting from the MEGA code is mainly perpendicular to the magnetic field. In the following sections, how this electric perturbation may cause fast-ion acceleration is discussed.

3.2. Full-orbit simulations of the fast ion distribution during an ELM

The ASCOT code [37] is employed to resolve the transport and acceleration of fast ions. ASCOT offers different methods to compute the Hamiltonian motion of minority species in tokamaks and stellarators. Its newest version, ASCOT5 [13], is a full rewrite in C, that uses OpenMP + MPI to leverage the capabilities of modern multi-threaded CPUs single-instruction multiple-data (SIMD) processes. In this work, we employed the full-orbit approach to simulate the fast-ion orbits, solving the equation of motion with a realistic three-dimensional description of the tokamak wall, enabling studies of fast-ion losses. The coupled effect of the fast ions on the electromagnetic perturbation, due to wave-particle interaction, is not considered in ASCOT. The effect of Coulomb collisions between the fast ions and the background plasma is disabled as the slowing-down time scales are above an order of magnitude higher than those simulated here. The markers are tracked in a time-dependent electromagnetic field, whose interpolator has been coded up in ASCOT5 during the course of this work [27]. The electromagnetic perturbation computed with MEGA from AUG shot #33616 at $t = 7.2\text{ s}$ is provided as an input to the time-dependent module, enabling the assessment of the fast-ion transport and acceleration during an entire ELM cycle.

The birth distributions of the 8 beams in AUG are modelled with the ASCOT5 particle generator, BBNBI5 [38], using 6 million markers for each beam. Each beamline, whose injection geometries and energies are described in section 2, provides a different birth profile in radius and pitch angle. Respectively, the initial energy fractions are 0.65%, 0.25%, 0.1% for primary, half and third injection energy from box 1 and 0.62%, 0.29%, 0.09% from box 2. The NBI-birth markers are first tracked in a separate ASCOT simulation with the MHD-quiescent equilibrium to filter out the NBI prompt losses. This makes it possible to isolate the effect of the ELM on the fast-ion distributions. The filtered distributions are then tracked during the unshaded time window of figure 5(a). As discussed, this time window is artificially stretched to 1.0 ms,

to obtain an ELM growth rate and duration more comparable to the experiments. The computed markers are launched altogether at the beginning of the ASCOT simulation to study the cumulative effect of the perturbation on the NBI-birth distribution. The ASCOT results show that, overall, 0.37% of the total markers are lost due to the ELM perturbation, corresponding to 0.40% of the total power, in agreement with FIDA measurements [19]. The patterns of the ELM-induced losses (excluding prompt losses) are shown in figure 6(a), projected onto the toroidal (φ) and poloidal (θ) angles on the wall. Apart from the lower divertor, the ELM-induced losses are mainly hitting the limiters near the midplane at the low field side, suggesting a strong impact from the ballooning structure of the perturbation. Simulations carried out with a 2D wall, thus avoiding any protuberance, show that the ELM-induced losses, whose projection in $\varphi - \theta$ can be observed in figure 6(b), follow the high- n , field-aligned patterns of the ELM perturbation. This result can be explained by the filamentary-like structure of the losses observed experimentally, as this pattern will populate different FILD probes in different times of the ELM crash. In these simulations, all the beams have produced similar patterns on the fast-ion losses, although the beams with lower pitch angles (passing orbits) produce slightly more losses.

During the ELM, a small fraction of the fast-ion distribution grows in energy, as can be observed in figure 7(a). These accelerated fast ions accumulate in the energy distribution forming a local maximum, as highlighted in figure 7(b) for the distribution of NBI1. A maximum at 92 keV in the fast-ion distribution can be seen after the ELM, which is ~ 30 keV above the primary injection energy of box 1, $E_0 = 60\text{ keV}$, the same order of magnitude as the acceleration observed in the experiments. As a result, the energy distribution contains an accelerated population above the primary NBI injection energy. The accelerated population is more clearly evident in the distributions of radial beams NBI1 and NBI4. These beams produce deeply trapped orbits in contrast with tangential beams which produce fast ions with passing orbits.

A synthetic signal for FILD can be constructed from the ASCOT results by computing the energy and pitch angle of the fast ions impinging on the FILD probe head. The synthetic signal produced by NBI1 on FILD2 is shown in figure 8(a). It depicts three distinguishable features at the primary (2.6 cm), half (1.8 cm) and third (1.5 cm) injection energy, broad in the pitch angle range. Additionally, there is a localized high-energy component at 3.5 cm and 81° . The high-energy feature is separated from the primary injection energy losses and its intensity is only an order of magnitude lower. This picture is in qualitative agreement with the tomographic inversion of the losses resolved in AUG experiments [5, 6]. However, the pitch angle of the high-energy feature seems to divert from the primary-energy losses towards more trapped values, which was not observed in the experiments. This feature is reproduced for several cases, as can be observed in figure 8(b), where the synthetic signal provided by a different fast-ion distribution (NBI4) produces the same qualitative result. The

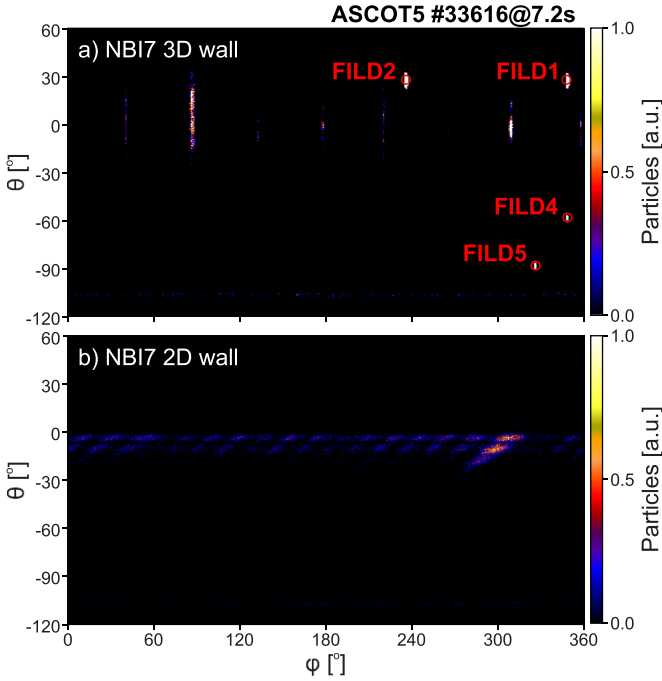


Figure 6. (a) ELM-induced fast-ion loss distribution on the AUG 3D wall calculated using ASCOT. (b) ELM-induced fast-ion loss distribution on the AUG 2D wall calculated using ASCOT. The distributions are projected in toroidal and poloidal angles. The fast-ion distribution is produced by NBI7 (off-axis).

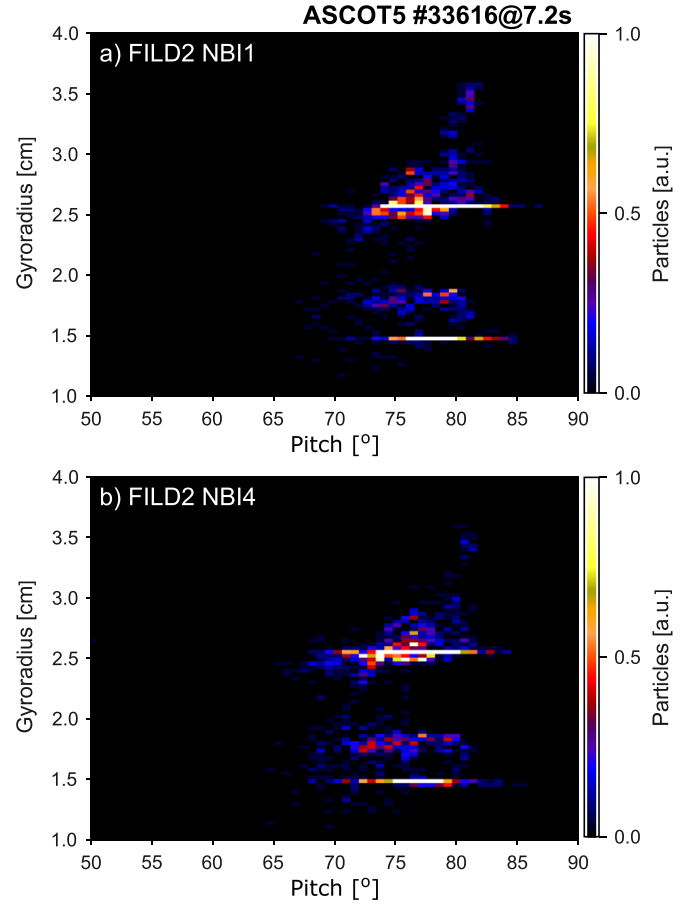


Figure 8. (a) Synthetic signal based on ASCOT simulations of FILD2 caused by ELM-induced fast-ion losses from NBI1. (b) Synthetic signal of FILD2 caused by ELM-induced fast-ion losses from NBI4.

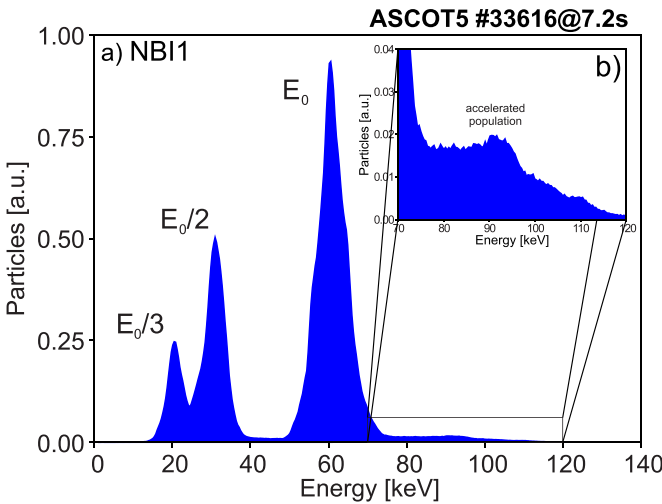


Figure 7. (a) Energy distribution of NBI1 after the ELM computed using ASCOT. (b) Zoom in of the accelerated population.

synthetic distributions from NBI1 and NBI4 produce a high-energy feature that can be numerically observed in both FILD1 and FILD2. The simulation does not deposit enough markers onto FILD3, 4 or 5 to produce a clear synthetic signal depicting the effect of the ballooning structure on the fast-ion loss deposition.

3.3. Fast-ion transport and acceleration mechanism

The fast-ion transport and acceleration during the ELM perturbation is assessed with ASCOT5 by tracking the values of two parameters that are constants of motion in the unperturbed fields. The particle toroidal canonical momentum is a constant of motion in axisymmetric magnetic fields and its variation (ΔP_φ) can be used as a measure of the radial transport produced by the magnetic perturbation [39]. The variation of the kinetic energy ($\Delta\varepsilon$) is an obvious measure of the acceleration

$$P_\varphi = mRv_\varphi - Ze\psi \quad (2)$$

$$\varepsilon = \frac{1}{2}mv^2 \quad (3)$$

where m is the particle mass, R the major radius, v_φ the toroidal component of the velocity, Ze the particle charge, ψ the poloidal flux and v the total velocity. To explore the fast-ion behaviour in phase-space, a set of markers with initial radial position, R , and pitch angle, Λ , are tracked in ASCOT5. The markers initial conditions are $\varphi = 0$, $z = 0$, $\varepsilon = 80$ keV. The

orbits are followed for $50 \mu\text{s}$. The electromagnetic perturbation is again provided by MEGA from AUG shot #33616 at $t = 7.2\text{s}$. The variation of P_φ and ε is evaluated at the time point in MEGA when the perturbation is maximum ($t = 0.125\text{ms}$). The variation of P_φ and ε is shown in figures 9(a) and (b), respectively. The patterns for different ELM times are similar to the ones presented here, with differences in the amplitude. Thus, these figures show the overall transport and acceleration pattern during the ELM. The first obvious conclusion inferred from figures 9(a) and (b) is that the particle transport and acceleration are localized at the edge, from $R = 2.05\text{m}$ ($\rho_{\text{pol}} = 0.84$) outwards, where the ballooning structure is the strongest, and beyond the separatrix. Also, it can be observed that the transport and acceleration follow different patterns. This is not unexpected, since $\delta\mathbf{B}$ is the dominant field perturbation that is responsible for the particle transport whereas the acceleration is caused entirely by $\delta\mathbf{E}$. As a consequence, both particle transport and acceleration will occur in a narrow phase-space region where the two effects overlap, as observed in previous investigations. Due to the different patterns in the transport and the acceleration, the two effects will be discussed separately.

The resonance condition between a fast-ion orbit and a perturbation in a tokamak plasma is given by [25, 26]:

$$\omega = n\omega_{\text{tor}} + p\omega_{\text{pol}} \quad (4)$$

where ω is the mode frequency, n the toroidal mode number, ω_{pol} is the orbit poloidal frequency, ω_{tor} is the orbit toroidal frequency and p is an arbitrary integer. For a static electromagnetic perturbation with a single toroidal mode number n , the geometrical resonance condition can be expressed in terms of the fraction $\omega_{\text{pol}}/\omega_{\text{tor}}$ [39]. In figure 9(a), the contour lines of the orbits $\omega_{\text{pol}}/\omega_{\text{tor}}$ are shown in white. It can be observed that the patterns in ΔP_φ follows the contour lines of $\omega_{\text{pol}}/\omega_{\text{tor}}$. This clearly suggests a resonant interaction between the fast ions and the magnetic perturbation, since the net transport is associated with specific values of $\omega_{\text{pol}}/\omega_{\text{tor}}$. In addition, fast ions are also affected by the chaotic field lines beyond $\rho_{\text{pol}} = 0.86$, shown in figure 10. The chaotic transport is mostly visible in the passing region of figure 9(a), producing blurry patterns in the ΔP_φ lines.

In contrast, the patterns in $\Delta\varepsilon$ do not clearly follow the contour lines of $\omega_{\text{pol}}/\omega_{\text{tor}}$. The reason is that the contour lines of $\omega_{\text{pol}}/\omega_{\text{tor}}$ represent resonance conditions with single- n perturbations, whereas the acceleration patterns are produced by an overlap of resonances with several dominant n values in the electric perturbation. This is illustrated in figure 9(c), where each n of $\delta\mathbf{E}$ is filtered and the $\Delta\varepsilon$ is calculated separately. The results show that the contour lines of $\Delta\varepsilon$ for each n adhere to the $\omega_{\text{pol}}/\omega_{\text{tor}}$ contour lines. In turn, when the $\Delta\varepsilon$ of each n are added up, the result is equivalent to figure 9(b), confirming the multi- n resonance overlap. These patterns are not observed in figure 9(a) because the magnetic field perturbation is dominantly $n = 20$.

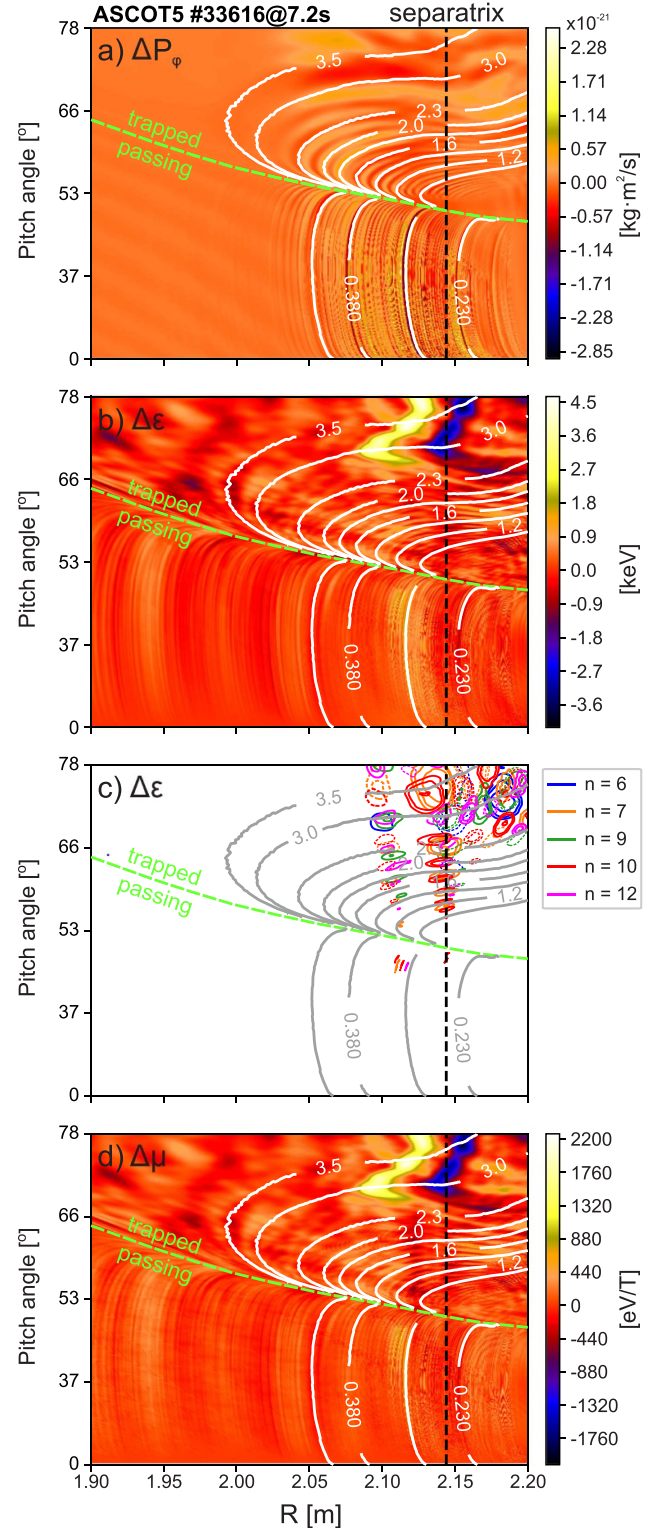


Figure 9. (a) Computed variation of the toroidal canonical momentum, ΔP_φ , during an ELM. Contour lines of $\omega_{\text{pol}}/\omega_{\text{tor}}$ are in white. (b) Computed variation of the kinetic energy, $\Delta\varepsilon$, during an ELM. Contour lines of $\omega_{\text{pol}}/\omega_{\text{tor}}$ are in white. (c) Contour lines of the variation of the kinetic energy produced by single- n electric perturbations. Negative values are shown as dashed lines. Contour lines of $\omega_{\text{pol}}/\omega_{\text{tor}}$ are in grey. (d) Computed variation of the magnetic moment, $\Delta\mu$, during an ELM. Contour lines of $\omega_{\text{pol}}/\omega_{\text{tor}}$ are in white.

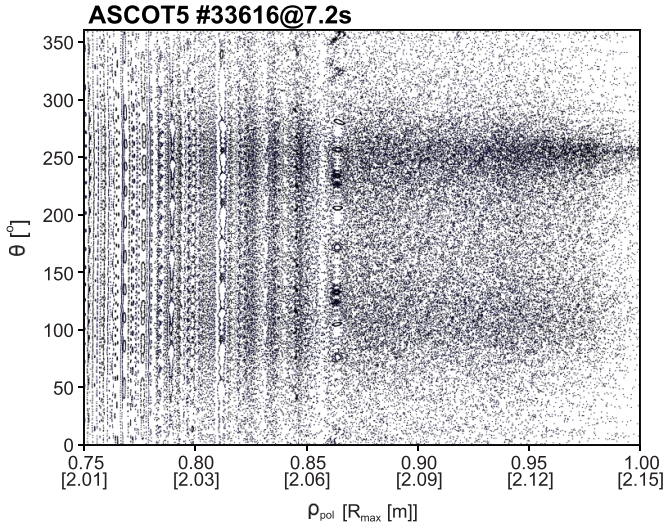


Figure 10. Computed Poincaré map of the perturbed magnetic field lines during the ELM. ρ_{pol} is the square root of normalised poloidal flux and θ is poloidal angle. Major radius of each ρ_{pol} marked in brackets.

The variation of the magnetic moment ($\mu = \frac{mv_{\perp}^2}{2B}$), an adiabatic invariant associated with the fast-ion gyroradius, reveals patterns that are analogous to those of the kinetic energy, as illustrated in figure 9(d). Changes in magnetic moment arise from field variations on the cyclotron scale [40], and therefore the similarity between figures 9(b) and (d) suggests strongly that the particle acceleration evident in the former is likely to be associated with sub-Larmor radius field fluctuations. As discussed before, the electric perturbation is dominated by the $\mathbf{v} \times \mathbf{B}$ term in Ohm's law, while the resistive term is 3 orders of magnitude lower. Therefore, the electric perturbation is mostly perpendicular to the magnetic field lines. It is known that perpendicular electric fields can cause acceleration if they change on the gyromotion time scale, breaking the magnetic moment invariance. While the frequency of the perturbation is too low to produce the necessary changes in the electric field, it has been noted that the electric perturbation changes spatially on the scale of the fast-ion gyroradii, as can be seen in figure 11. This produces a net variation in the magnetic moment along the fast-ion gyromotion, that results in a gyrotron acceleration due to orbit drift resonances with the electric perturbation. To verify this, analogous guiding centre simulations have been carried out, as this approach neglects any effects on gyromotion time scales. The guiding centre simulations show an energy gain below 0.5 keV, in contrast to the 4.5 keV energy gain observed in full orbit simulations. This indicates that the electric field perturbation is causing acceleration on gyromotion scales. Two clear regions of positive and negative $\Delta\epsilon$ can be observed in figure 9(b), correlated with the side of the gyromotion that is affected positively or negatively by the electric field. Since the negative $\Delta\epsilon$ region is outside the separatrix, where there are fewer fast ions, only fast-ion acceleration is observed in the simulations as well as in the experiments.

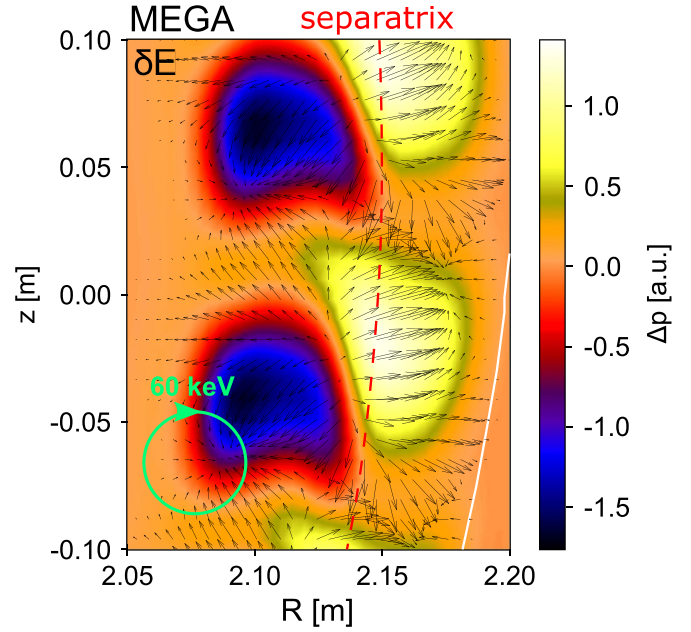


Figure 11. Computed pressure perturbation during the ELM (colour bar) and $\delta\mathbf{E}$ vector field (arrows, with the length of the arrow indicating the magnitude of the field) near the edge. The gyromotion of a 60 keV deuterium ion is shown for reference.

4. Discussion

The experimental results in ASDEX Upgrade have demonstrated that type-I ELMs have a negative impact on fast-ion confinement [5, 6, 17]. The ELM-induced losses exhibit variations in the toroidal and poloidal directions that suggest a field-aligned pattern of the fast-ion losses. Also, velocity-space measurements of the fast-ion losses have revealed losses at energies above the beam injection energy, suggesting that fast ions are accelerated by the ELM perturbation. A new statistical analysis reveals that the fast-ion losses are proportional to the magnetic perturbation during the ELM crash and the divertor current, suggesting strongly that the magnetic perturbation is responsible for enhancing the fast-ion losses.

With the aim of studying the transport and acceleration induced by the type-I ELMs, the electromagnetic perturbation has been modelled with the MHD module of the hybrid kinetic-MHD code MEGA and then fed to a time-dependent module of the orbit tracing code ASCOT5 to study the effect on the fast-ion distribution. This has been a major improvement on previous work, as it uses MHD-resolved time-evolving electromagnetic perturbations to trace the fast-ion orbits, instead of an analytical static model of the perturbation. The results show that 0.4% of the total fast-ion power is lost during an ELM, in line with previous FIDA measurements [19]. Although the power loss is relatively low, the modelled fast-ion losses reveal field-aligned patterns with a periodicity matching the dominant n number of the magnetic perturbation, condensing the power load on localised regions of the wall that

might endanger it. The modelled confined fast-ion distribution includes an accelerated population above the injection energy, that could be observed in the synthetic FILD signal. In sum, the model qualitatively reproduces the main experimental observations. However, the model reproduces these features more clearly with NBI1 and NBI4 distributions, in contrast to those used in the experiments (NBI7 and NBI8). In fact, it can be observed that the main pitch angle ($\Lambda_{NBI1} = 78^\circ$ and $\Lambda_{NBI4} = 75^\circ$) of these NBI sources are more resonant with the modelled perturbation than those of the sources used in the experiments ($\Lambda_{NBI7} = 45^\circ$ and $\Lambda_{NBI8} = 63^\circ$). The fact that the dominant n number is considerably higher in the model than in the experiments, which is known to have a strong impact on the dynamics of the fast-ion interaction with the instability [5, 6], could help to explain why different NBI distributions are affected in the model. Moreover, the timescale of the electromagnetic perturbation computed by MEGA is stretched to achieve similar growth rates to those reported experimentally. Simulations without the stretch of the perturbation lead to results difficult to interpret as the particles do not have enough time to interact with the mode. While this is evidence of the resonant interaction between the fast ions and the perturbation, future studies should address the effect of the ELM growth rate of the fast-ion transport and acceleration. The ELM-induced losses computed with ASCOT were considerably lower in FILD3 and FILD5, in agreement with the experiments. These are the probes that are more separated from the midplane, evidencing that the fast-ion losses are distributed along the LFS midplane driven the ballooning structure of the ELM.

A parametric study of the fast-ion phase-space reveals that the fast-ion transport is caused by a resonant interaction with the magnetic perturbation, in line with the experimental analysis. Simulating a 3D electric perturbation makes it possible to study the contribution of the parallel and perpendicular electric fields on the fast-ion acceleration. The acceleration is produced by a resonant interaction with the perpendicular $\mathbf{v} \times \mathbf{B}$ electric perturbation, whose gradient with scales smaller than the fast-ion gyroradius breaks the conservation of the magnetic moment. This contrasts with the hypothesis of acceleration due to a parallel electric field proposed in previous work. However, the acceleration process may involve a combination of both electric fields. It has been noted that the acceleration due to a parallel electric field decreases the fast-ion pitch angle, while the perpendicular electric field increases it. The experimentally-observed accelerated fast ions have pitch angle values similar to those of the NBI prompt losses. Therefore, a combination of parallel and perpendicular electric field must play a role in the acceleration of fast ions to keep a roughly constant pitch angle, if we assume that the accelerated losses are sourced from the prompt-loss population measured by the FILD. These conclusions are in line with the proposed acceleration of energetic particles due to propagating plasma blobs [10], where vertically polarized blobs with sizes smaller than the fast-ion gyroradius would produce parallel and perpendicular electric fields that interact with the fast particle gyromotion thus accelerating them.

In conclusion, the process by which ELMs induce fast-ion transport and acceleration has been modelled, showing a

resonant interaction between the fast-ion orbits and the electromagnetic perturbation arising during an ELM. Future work should address the diamagnetic effects on the ELM evolution with the aim of replicating mode numbers and growth rates observed in the experiments and assessing their effect on the fast ions. Similarly, the effect of the fast ions on the ELM stability is not yet understood and has not been included in these models, so it remains a key question for future study. The observations are still to be reproduced in other machines. For instance, dedicated experiments to study the ELM-induced fast-ion losses are being carried out in MAST-U, as it is equipped with a FILD probe with enough spatial and temporal resolution to resolve the intra-ELM fast-ion loss velocity space [16], and in JET, where the absolute calibration of FILD will make it possible to characterise the ELM-induced fast-ion losses in terms of ions per second [41].

Acknowledgments

This work has been carried out within the framework of the EUROfusion Consortium, funded by the European Union via the Euratom Research and Training Programme (Grant Agreement No. 101052200—EUROfusion) and from the EPSRC [Grant Number EP/W006839/1]. To obtain further information on the data and models underlying this paper please contact PublicationsManager@ukaea.uk. Views and opinions expressed are however those of the author(s) only and do not necessarily reflect those of the European Union or the European Commission. Neither the European Union nor the European Commission can be held responsible for them.

This research received funding from the V Plan Propio de Investigación de la Universidad de Sevilla (PP2016-7145).

This project has received funding from the European Research Council (ERC) under the European Union's Horizon 2020 research and innovation programme (Grant Agreement No. 805162).

The simulations were partly performed on the MARCONI supercomputer (CINECA).

J. Galdon-Quiroga acknowledges support from the MSCA PF programme under Grant No. 101069021.

ORCID iDs


J.F. Rivero-Rodríguez  <https://orcid.org/0000-0001-5074-0267>

J. Galdon-Quiroga  <https://orcid.org/0000-0002-7415-1894>

M. García-Muñoz  <https://orcid.org/0000-0002-3241-502X>

K.G. McClements  <https://orcid.org/0000-0002-5162-509X>

L. Sanchís  <https://orcid.org/0000-0001-8211-3356>

K. Särkimäki  <https://orcid.org/0000-0001-9156-2559>

A. Snicker  <https://orcid.org/0000-0001-9604-9666>

Y. Todo  <https://orcid.org/0000-0001-9323-8285>

E. Viezzer  <https://orcid.org/0000-0001-6419-6848>

References

- [1] Connor J.W. 1998 *Plasma Phys. Control. Fusion* **40** 531–42
- [2] Zohm H. 1996 *Plasma Phys. Control. Fusion* **38** 105
- [3] Loarte A. *et al* 2007 *Phys. Scr.* **128** 222–8
- [4] Eich T., Sieglin B., Thornton A.J., Faitsch M., Kirk A., Herrmann A. and Suttrop W. 2017 *Nucl. Mater. Energy* **12** 84–90
- [5] Galdon-Quiroga J. *et al* 2018 *Phys. Rev. Lett.* **121** 025002
- [6] Galdon-Quiroga J. *et al* 2019 *Nucl. Fusion* **59** 066016
- [7] Leonard A.W. 2014 *Phys. Plasmas* **21** 090501
- [8] Helander P., Eriksson L.-G., Akers R.J., Byrom C., Gimblett C.G. and Tournianski M.R. 2002 *Phys. Rev. Lett.* **89** 235002
- [9] Freethy S.J., McClements K.G., Chapman S.C., Dendy R.O., Lai W.N., Pamela S.J.P., Shevchenko V.F. and Vann R.G.L. 2015 *Phys. Rev. Lett.* **114** 125004
- [10] Marchenko V.S. and Reznik S.N. 2018 *Phys. Plasmas* **25** 084502
- [11] Todo Y. and Sato T. 1998 *Phys. Plasmas* **5** 1321–7
- [12] Todo Y., Seki R., Spong D.A., Wang H., Suzuki Y., Yamamoto S., Nakajima N. and Osakabe M. 2017 *Phys. Plasmas* **24** 081203
- [13] Varje J. *et al* 2019 High-performance orbit-following code ASCOT5 for Monte Carlo simulations in fusion plasmas (arXiv:1908.02482)
- [14] Zweben S.J. 1989 *Nucl. Fusion* **29** 825–33
- [15] García-Muñoz M., Fahrbach H.-U. and Zohm H. 2009 *Rev. Sci. Instrum.* **80** 053503
- [16] Rivero-Rodríguez J.F. *et al* 2018 *Rev. Sci. Instrum.* **89** 101112
- [17] García-Muñoz M. *et al* 2013 *Plasma Phys. Control. Fusion* **55** 124014
- [18] Jansen van Vuuren A., Geiger B., Jacobsen A.S., Cavedon M., Dux R. and Köhnlein H. 2019 *Rev. Sci. Instrum.* **90** 103501
- [19] Jansen van Vuuren A., Geiger B., Schneider P.A., Bogar K., Poloskei P.Z., Cathey A., Hoelzl M., Jacobsen A.S., Cavedon M. and Dux R. (The ASDEX Upgrade Team) 2021 *Nucl. Fusion* **61** 046001
- [20] Gonzalez-Martin J. *et al* 2018 *Rev. Sci. Instrum.* **89** 101106
- [21] Gonzalez-Martin J. *et al* 2019 *J. Instrum.* **14** C11005
- [22] Gonzalez-Martin J. *et al* 2021 *Rev. Sci. Instrum.* **92** 053538
- [23] Galdon-Quiroga J. *et al* 2018 *Plasma Phys. Control. Fusion* **60** 105005
- [24] Rivero-Rodríguez J.F. *et al* 2019 *J. Instrum.* **14** C09015
- [25] Zonca F., Chen L., Briguglio S., Fogaccia G., Vlad G. and Wang X. 2015 *New J. Phys.* **17** 013052
- [26] Chen L. and Zonca F. 2016 *Rev. Mod. Phys.* **88** 015008
- [27] Rivero-Rodríguez J. 2021 Fast-ion transport and acceleration induced by edge localized modes in MAST Upgrade and ASDEX Upgrade *PhD Thesis* Universidad de Sevilla
- [28] Mink F., Wolfrum E., Maraschek M., Zohm H., Horváth L., Laggner F.M., Manz P., Viezzer E. and Stroth U. 2016 *Plasma Phys. Control. Fusion* **58** 125013
- [29] Dominguez-Palacios J. *et al* 2023 Hybrid kinetic MHD multi-n simulations of ELMs in the ASDEX Upgrade tokamak with MEGA 3rd Spanish HPC Fusion Workshop (Barcelona, Spain, 5–16 December 2022) (available at: <https://hpcfusion.bsc.es/2022/>)
- [30] Bierwage A., Shinohara K., Todo Y., Aiba N., Ishikawa M., Matsunaga G., Takechi M. and Yagi M. 2018 *Nat. Commun.* **9** 3282
- [31] Dominguez-Palacios J. *et al* 2019 Non-linear 3D hybrid kinetic-MHD simulations of ELMs in the ASDEX Upgrade tokamak with MEGA 16th Technical Meeting on Energetic Particles in Magnetic Confinement Systems—Theory of Plasma Instabilities (Shizuoka City, Japan, 3–6 September 2019) (available at: <https://conferences.iaea.org/event/185/>)
- [32] Mink F. *et al* 2018 *Nucl. Fusion* **58** 026011
- [33] Hoelzl M. *et al* 2018 Simulating tokamak edge instabilities: advances and challenges 45th EPS Conf. on Plasma Physics (Prague, Czech Republic, 2–6 July 2018) (available at: <http://ocs.ciemat.es/EPS2018PAP/html/contrib.html>)
- [34] Sato M., Nakajima N., Watanabe K.Y. and Todo Y. 2017 *Nucl. Fusion* **57** 126023
- [35] Cathey A., Hoelzl M., Lackner K., Huijsmans G.T.A., Dunne M.G., Wolfrum E., Pamela S.J.P., Orain F. and Günter S. 2020 *Nucl. Fusion* **60** 124007
- [36] Isliker H., Cathey A., Hoelzl M., Pamela S. and Vlahos L. 2022 *Phys. Plasmas* **29** 112306
- [37] Hirvijoki E., Asunta O., Koskela T., Kurki-Suonio T., Miettunen J., Sipilä S., Snicker A. and Äkäslompolo S. 2014 *Comput. Phys. Commun.* **185** 1310–21
- [38] Asunta O., Govenius J., Budny R., Gorelenkova M., Tardini G., Kurki-Suonio T., Salmi A. and Sipilä S. 2014 *Comput. Phys. Commun.* **188** 33–46
- [39] Sanchis L. *et al* 2018 *Plasma Phys. Control. Fusion* **61** 014038
- [40] Kaufman A.N. 1972 *Phys. Fluids* **15** 1063–9
- [41] Rivero-Rodríguez J.F. *et al* 2021 *Rev. Sci. Instrum.* **92** 043553